

Figure 4.15 Real-time variation of PEGDA/GO resistance during UV irradiation, starting from as-printed non-polymerized material (time = 0), for three different UV light power densities

during UV light irradiation with power density of  $85 \text{ mW/cm}^2$ , for both the pure PEGDA polymeric matrix and the PEGDA/GO composite. The higher the thickness, the lower the line resistance. The electrical measurements performed in situ during the step of polymer cross-linking/GO reduction allowed to monitor the mechanism of reaction which led to the reduction of the overall resistivity of the printed composite toward the values measured for the pure polymer matrix. Figure 4.16 reports the variation of sample resistance with time, during UV light irradiation with power density of  $85 \text{ mW/cm}^2$ , for both the pure PEGDA polymeric matrix and the PEGDA/GO composite.

The values registered at time=0 correspond to the as-printed non-polymerized samples. The resistance of the pure PEGDA matrix before UV irradiation is quite low, due to the fact that the electrical signal can be carried via ionic diffusion in a quasiliquid matrix. As soon as the cross-linking of polymer chains is achieved, a few seconds after UV light irradiation begins, the resistance of the matrix abruptly increases by several orders of magnitude, until the point in which the complete polymerization, reached after about a minute of irradiation, reveals the dissipative behavior that is an intrinsic characteristic of the polymer (the resistivity of fully cross-linked PEGDA is around  $10^6 \times \text{cm}$ ). Conversely, the resistance of the sample containing

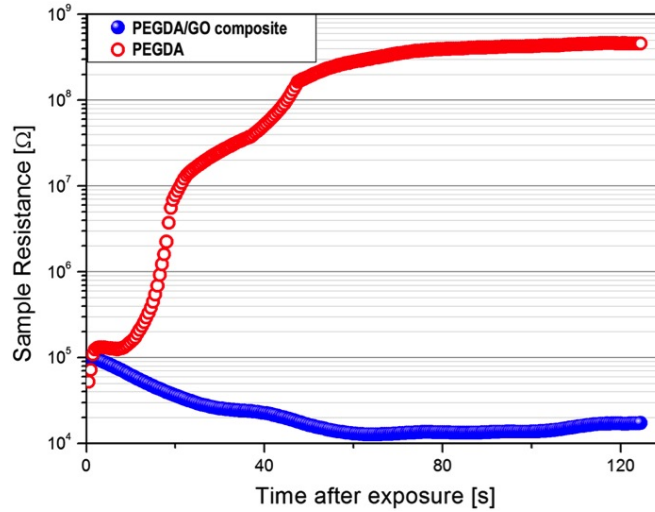


Figure 4.16 Real-time variation of sample resistance during UV irradiation for pure PEGDA polymeric matrix (upper red line) and the PEGDA/GO composite (lower blue line), starting from as-printed non-polymerized material (time = 0)

GO decreases during the photo-polymerization of the matrix, until at complete cross-linking a slight resistance increase is recorded. This effect is clearly due to the presence of the filler, which is reduced by the interaction with photoinitiator radicals promoted by the UV light irradiation, to form conductive graphene clusters. These act as preferential pathways for the mobility of charge carriers, thus leading to an overall decrease of the materials resistance despite the concurrent cross-linking of the polymeric matrix.

After about 170 s of UV irradiation at the highest UV light power density (85 mW/cm<sup>2</sup>), the values of resistance come back to a slight increase. It can be speculated that this is probably the point in which most functionalities on the surface of graphitic sheets have been reduced, while the ionic mobility and interchain hopping in the acrylic resin are further inhibited by the cross-linking of the polymer insulating chains.

### 4.2.3 Preliminary Piezoresistive Measurements

Aim of this work is the realization of flexible pressure sensors for robotic applications, which require metal-free, cost-effective, easily processable materials, featuring high sensitivity and linear response in order to realize a network of sensing areas. In this specific case, a sensing

skin is conceived to mimic the human skin both in terms of force sensitivity and mechanical stiffness, resulting in strong constraints in the choice of materials. Graphene allows to match the requirements of force sensitivity, mechanical stiffness, easily processable material and linear response, when coupled to the proper polymeric matrix required for piezoresistive devices.

#### 4.2.3.1 Materials and Methods

Polymer based nanocomposites were prepared by solvent casting in order to obtain samples with controlled size and thickness, as described in Figure 4.17, featuring a dispersion of graphene oxide (GO) in three different matrices: polyethyleneglycol diacrylate (PEGDA), soft biocompatible polydimethylsiloxane (PDMS) and 2-bromoethyl methacrylate (BEMA, average  $M_n=1700$ , Aldrich) with the photo-initiator was 2-hydroxy-2-methyl-1-phenyl-1-propanon (Darocur 1173, Ciba Specialty Chemicals). Piezoresistive sensors were fabricated by coating flexible electrodes, consisting of metalized polyimide sheets, with the polymer/GO composites. After coating, GO was reduced to graphene by UV irradiation and brought to a conductive regime, allowing in some cases the simultaneous photopolymerization of resin matrices, where applicable (PEGDA, BEMA).

Finally the samples were assembled by contacting them with conductive copper tape and kapton scotch to fix and isolate the wires.

Electrical (I-V curves) and piezoresistive characterization of flexible sensors were then per-

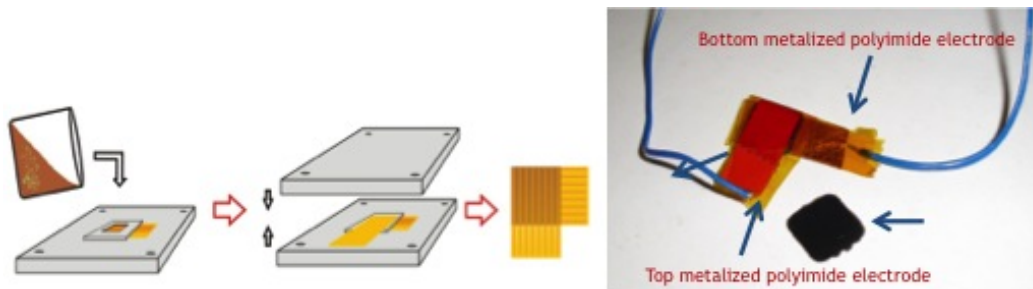


Figure 4.17 Piezoresistive samples preparation method.

formed. In particular, the samples were tested by submitting them to a uniaxial compression

in the range 0-1 MPa and the experimental data were fitted using the Farazdaghi–Harris model.

#### 4.2.3.2 Results and Discussion

Preliminary piezoresistive measurements for pressure sensor applications were also performed on the thick samples of graphene compounds. BEMA, which can be photopolymerized by a photoreactive initiator under UV light irradiation, was also used in order to create a different graphene compound and compare the piezoresistive characteristic with the PEGDA, and compound with different load of graphene oxide in PEGDA were also prepared. The representation  $R$  vs  $p$  in Figure 4.18 gives curves that are the mean between 3 measures composed by an up cycle (increasing pressure) and a down one (decreasing). The local resistance minimum found around 2 bars is an effect connected to the overall resistance increase produced by ageing. A fast viscoelastic recovery in PEGDA samples prevents from directly measuring this anomaly (this doesn't apply to BEMA).

Increasing the rGO amount increases hysteresis, and the samples with BEMA have better performance with a lower hysteresis and noise. PEGDA and BEMA show a piezoelectric effect linear plus a nonlinear effect possibly depending on viscoelasticity. PDMS nanocomposites were also tested and in Figure 4.19 are shown extremely high resistance values ( $T\Omega$ ) comparable to internal resistance of multimeter (Keithley 2635A). These preliminary results led to the conclusions that the PDMS nanocomposites feature an extremely high resistance which is not compliant with the internal resistance of standard instruments, making it very difficult to measure it. Both pure PEGDA and BEMA show a piezoelectric effect (linear plus a nonlinear effect possibly depending on viscoelasticity). The PEGDA nanocomposites feature a high hysteresis at very low applied pressures and also at high pressures depending on the rGO amount (less is better), in any case featuring a poor repeatability and confidence belts that grow from some percent up to 400% at 7 bar. Finally, the BEMA nanocomposites feature a reduced hysteresis both at low and high pressures with a reduced confidence belt, when compared to PEGDA composites, showing an improved repeatability.

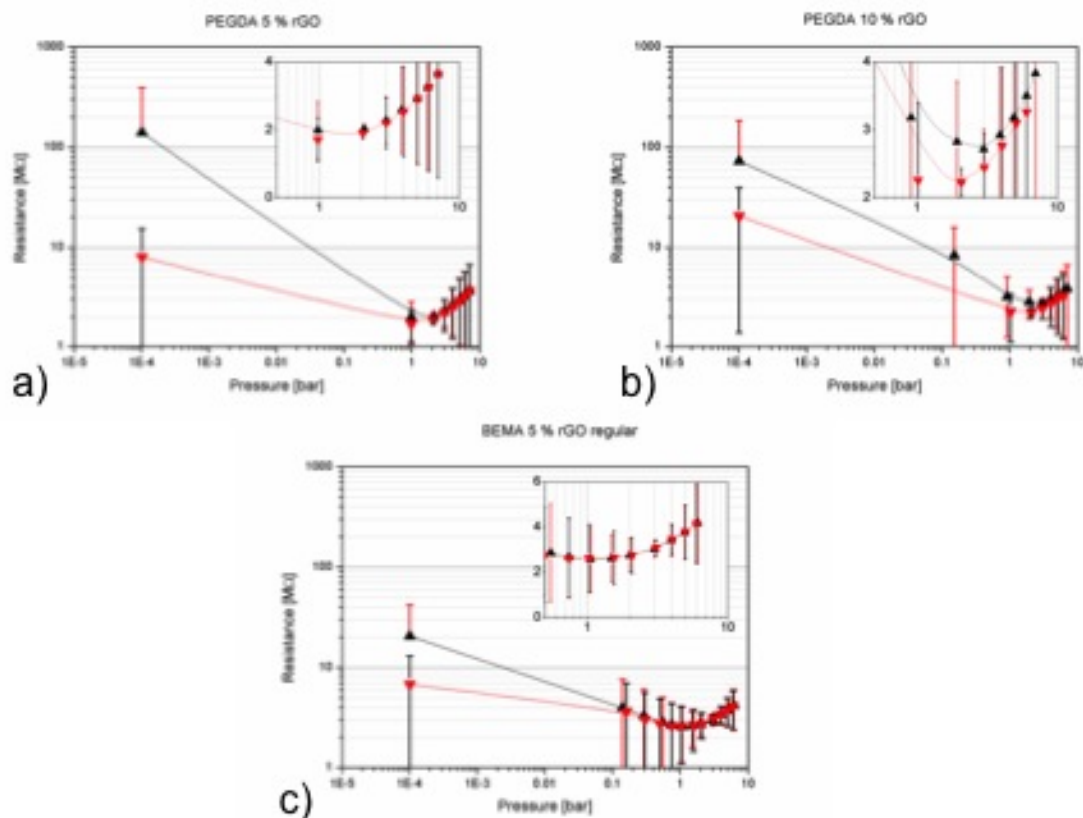


Figure 4.18 Piezo resistive measurements, (a) PEGDA 5% rGO, (b) PEGDA 10% rGO and (c) BEMA 5% rGO.

### 4.3 Conclusion

A route to obtain inkjet printable, environmentally friendly inks based on graphene/acrylic nanocomposites was presented. The excellent rheological characteristics of the formulations warranted printability with good repeatability. The concurrent UV-driven polymerization of PEGDA matrix and reduction of graphene oxide filler was verified by XPS analysis. Thin printed samples of the nanocomposite showed a decrease of resistivity by two orders of magnitude with respect to the pure matrix. In particular, it was observed that the resistivity of thin layers was much lower than one of the thick layers. This effect is ascribed to the formation of free radicals, which may have a role in the reduction of graphene oxide, from the photo-initiator used to start the polymerization of the matrix. This reaction is proportional to the amount of

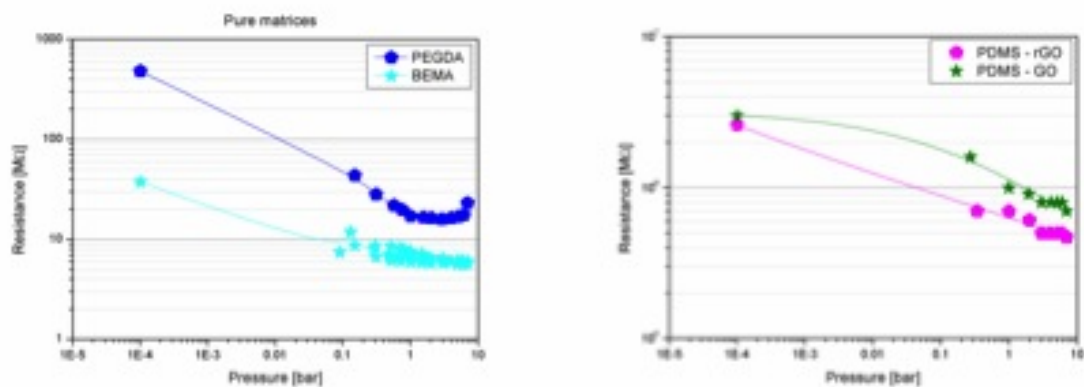


Figure 4.19 Piezo resistive measurements, (a) pure matrices PEGDA and BEMA and (b) PDMS with GO and rGO.

incoming UV light, therefore it is more effective in thin layers, where the light penetration is higher than in thick layers.

## **Chapter5. GRAPHENE BASED ELECTRODES FOR SUPERCAPACITOR APPLICATIONS**

In this chapter successful results of the synthesis and characterizations of novel graphene based composites obtained for energy storage applications will be presented. In the first part a brief overview on different materials and their properties used as electrodes for energy storage devices will be introduced, while in the second part several graphene composites materials that have been synthesized and characterized will be presented and discuss in detail. The goal of this investigation was of obtaining materials with good electrochemical performance that could also be environmentally friendly, non toxic and low cost.

The most successful composites obtained through the use of hydrothermal synthesis that combined graphene with other material will be presented. The first material that will be introduced is a composite with a metal oxide: the molybdenum dioxide; which gave the highest value of specific capacitance among the materials investigated, by exploiting the intercalation of sodium ion. Other two composites obtained with hydrothermal synthesis will be then introduced; one with another non toxic metal oxide: titanium oxide, and the other with the expanded graphite as partial substitute of the graphene oxide in order to lower the overall cost of the electrodes. Finally a graphene/sodium silicate composite will be proposed through an in situ synthesis and reduction process. Morphological, compositional and electrochemical characterizations of all the material investigated are reported and discussed in detail.

## 5.1 Background

Energy storage holds the promise to provide a variety of benefits across the entire energy delivery value chain ranging from generation to delivery (transmission and distribution) to consumption (154), (155). While a number of different types of storage technologies exist today, electrochemical method has been dominated for consumer related applications (156). Electrochemical energy storage, in general, relies on two types of devices, namely batteries and capacitors. A common component of two devices is the electrodes, which connect the external electric circuit to the internal electrochemical cell. The materials, structures and performance of the electrodes, therefore, have been of great interest of researches on two devices (160), (159). Carbons have been recognized as a popular electrode material due to their abundance, wide electrochemical window, and low cost, etc. Indeed a variety of carbons (glassy carbon, graphite, carbon black powder, carbon nanotube, graphene, etc.) have been studied as the electrodes of electrochemical cells (157), (158). In addition, hybrid materials containing carbon as a backbone have been widely explored as well (161).

The hybridization (for example hybridization of carbon with metal oxides) often results in improvements of material performance such as stability, catalytic activity, conductivity, and so on (165). Supercapacitors can be classified in three categories based on different ways of storing power: Electric Double Layer Capacitor (EDLC), Pseudocapacitor, and Hybrid (from the combination of the first two categories) as shown in Figure 5.1. Supercapacitors as the Electric Double Layer Capacitor (EDLC) are generally fabricated using carbon-based materials, like carbon black, carbon aerogels (161), carbon nanotubes or graphene (162), combined to other materials like metal oxides or conductive polymers, that supply an additional contribution to the total capacitance value (163). The capacitance of EDLCs is generated from the separation of charges at the interface between the electrode and the electrolyte (known as the Helmholtz layer) as represented in Figure 5.2.

EDLC have very high cyclic stability but a lower value of capacitance with respect to the other two categories. Supercapacitors based on the pseudocapacitance effect can generate capacitance from rapid Faradaic reactions, such as surface redox, intercalation, and electro-sorption pro-

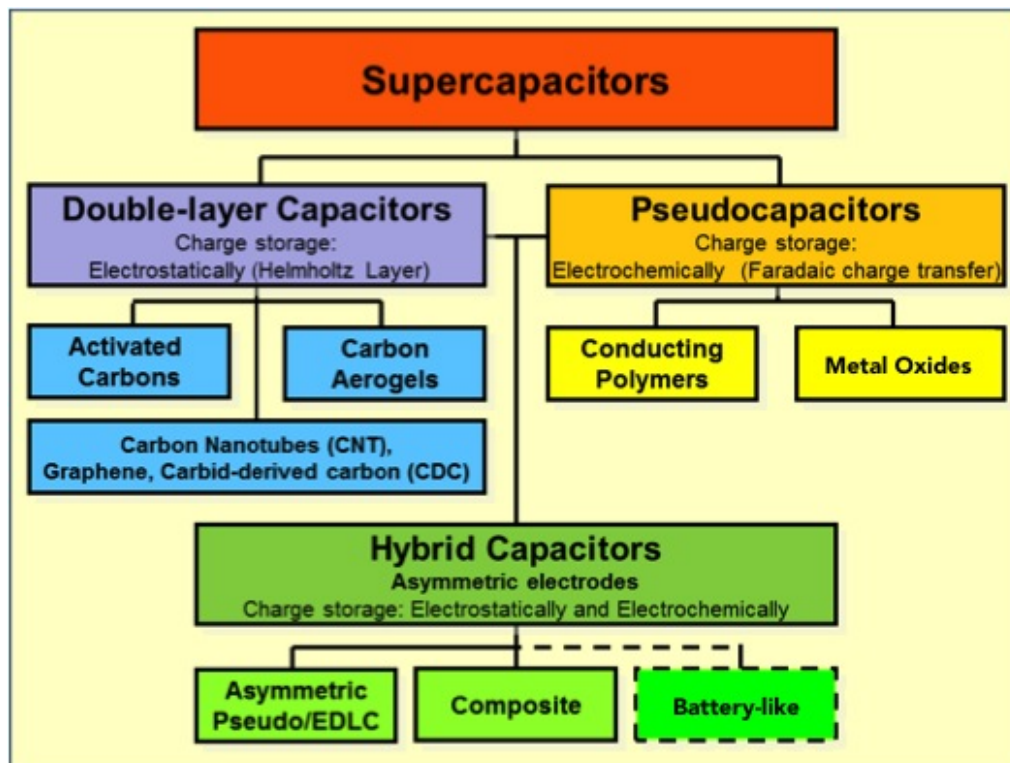


Figure 5.1 Supercapacitors types scheme.

cesses at high surface area electrodes such as metal oxides and conducting polymers. This type of supercapacitor is able to generate a higher capacitance than the EDLC, but suffers from a poorer cyclic stability (163). Recently developed, a new class of supercapacitors called hybrids has the purpose of combining the advantages of batteries with those of the other two categories of supercapacitor. Hybrid supercapacitors consist in a combination of a Faradaic battery-like electrode (featuring a pseudo-capacitive metal oxide or Li insertion) coupled with a capacitive carbon electrode, and they exploit a double effect given by the capacitance and the battery-like electrode where the energy can be stored (164).

In the last few years, a renewed interest in sodium (Na) ion batteries has also been raised as an alternative to Li (Li) ion batteries, due to the scarce availability of Li in terms of natural resources, and other technical difficulties that resulted from the many issues in safety and handling of the material, and in the recycling processes (165). A particular interest concerning the research on Na-ion batteries has been raised about negative electrode materials that could intercalate Na ions (166), (167). Moreover, even though much research effort was focused in

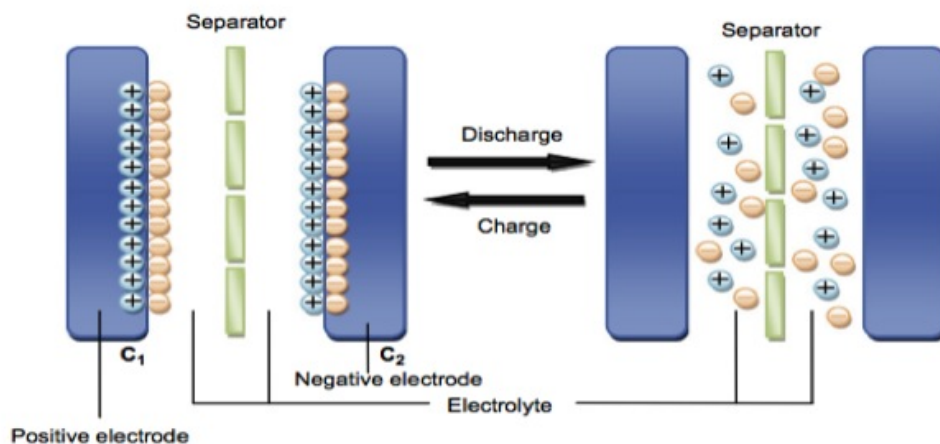


Figure 5.2 EDLC charge/discharge schematic representation.

the field of Li-ion batteries with growing competitiveness, future directions for increasing the energy density of those devices through new chemistry remain unclear (167), (192).

Graphene and graphene-derived materials have been largely studied and employed in the fabrication of electrodes (169), because of their outstanding chemical and physical properties including superior electrical conductivity, large surface area, chemical and thermal stability, ultrathin thickness, high mechanical flexibility and strength, and broad electrochemical window (170), (171). In particular, the methods for hydrothermal synthesis were proven to be clean, easy, environmentally friendly and scalable techniques to obtain high surface area reduced graphene oxide (RGO), starting from simple dispersions of graphene oxide (GO) in water (172), (85). Using these methods, it is possible to obtain the reduction of GO and the concurrent formation of a complex high surface area structure that self-assembles in strong and elastic aggregation of networks.

Metal oxides like the molybdenum dioxide ( $\text{MoO}_2$ ) have been recently studied for their electrochemical properties, in particular for the intercalation of Li-ions (174) and in supercapacitors (175). This work presents the study of novel electrodes for hybrid supercapacitors that exploits the intercalation of Na ions. The main goal in the fabrication of this device was the improvement of the capacitance values, exploiting the high surface area of the conductive nanostructured carbon electrodes combined with a pseudocapacitance effect arising from the metal oxide com-

ponent. A comprehensive study of the Na ions intercalation in the metal oxide was achieved through structural and morphological characterization of the synthesized materials.

## 5.2 Experimental Session

### 5.2.1 Hydrothermal Synthesis of rGO/Molybdenum Dioxide Composites

In this section, the synthesis and electrochemical characteristics of a carbon hybrid, which contains molybdenum (IV) oxide ( $\text{MoO}_2$ ) are presented and discussed. Hydrothermal synthesis, which provides a reduced graphene oxide (RGO) and molybdenum (IV) oxide hybrid through a facile one-pot process was used as synthesis technique. The structure of the hybrid material was carefully characterized using electron microscopy (SEM and TEM), x-ray diffraction (XRD), x-ray photoelectron spectroscopy (XPS) and micro-Raman spectroscopy. The hybrid was applied to a supercapacitor containing symmetric electrodes with an aqueous electrolyte of sodium ions ( $\text{Na}^+$ ) and its electrochemical performance along with  $\text{Na}^+$  ion insertion in aqueous electrolyte are then going to be discussed. The idea behind the choice of the hydrothermal synthesis as fabrication process of supercapacitor electrode materials stands in the fact that it is possible to achieve good composite materials with high surface area through the formation of a porous structure, that is capable to host ions and offer a very high number of ways for their mobility.

In particular, graphene/ $\text{MoO}_2$  compounds has been already reported in literature and tested as electrode materials for Li-ion batteries (176), (177). In addition, also molybdenum trioxide ( $\text{MoO}_3$ ) was recently studied, due to the possibility of intercalation of Na ions, owing to its orthorhombic crystalline phase that allows enough space for Na ions to intercalate between the crystalline planes (178), (179), and Graphene/ $\text{MoO}_3$  was also reported for application in Li-ion battery cathodes (180), (181).

In all the experiments performed the RGO/ $\text{MoO}_2$  compounds were used as intercalating material for Na ions.  $\text{MoO}_2$  was preferred to  $\text{MoO}_3$  as electrode material because of its conductive and non toxicity properties (182). In addition, it was proved that its monoclinic crystalline

structure could also host Na as well as Li ions (193),(194).

### 5.2.1.1 Materials and Methods

Commercial reagents were used without further purification. Graphene oxide (thickness 0.7-1.2 nm) was purchased from ACS Materials (USA). Phosphomolybdic acid (PMA) solution of 20 wt.% in ethanol, poly(tetrafluoroethylene) (PTFE), and  $\text{Na}_2\text{SO}_4$  were purchased from Sigma-Aldrich. Deionized (DI) water was used as a solvent for the electrolyte.

The graphene oxide (GO) powder was dispersed in DI water at room temperature using a Branson ultrasonic bath cleaner until the particulates were not visible. 0.5 g of PMA solution was added to the GO in DI water dispersion (2 mg/ml for 12 ml total volume) and ultrasonicated for 15 minutes. After sonication, the solution was transferred in a Teflon lined stainless steel autoclave with total volume of 18 ml and placed in a vacuum oven at a temperature of 180°C for 16 hours. After the hydrothermal reaction, when the autoclave reached room temperature, the samples were frozen using liquid nitrogen and dried overnight under vacuum. Samples with only graphene oxide were also prepared with the same procedure as comparison with the composite samples.

The morphology and structure of the hybrid synthesized by the hydrothermal method were investigated using a FEI Helios Nanolab 400S field emission FIB/SEM and, an JEOL JEM-ARM200F STEM Cs-corrected cold FEG atomic resolution analytical microscope with GIF Quantum post column energy filter and JEOL Centurio SDD EDS (silicon drift detector energy dispersive spectrometer). All EELS spectra were taken at 1 eV/channel dispersion. For X-ray photoelectron spectroscopy (XPS), a Physical Electronics Quantum ESCA Microprobe, using a monochromated Al  $K\alpha$  X-ray source, 200 mm spot size throughout and charge neutralization was used. 1000 eV survey spectra (187 eV pass energy, 1.6 eV/step) and high-resolution spectra (47 eV PE, 0.4 eV/step) were obtained. The crystalline phase was analyzed with a Bruker D8 Discover X-ray diffractometer fitted with a 2-dimensional (2D) X-ray detector. All scans were performed with the detector and incident beam in a symmetric  $\theta$ - $2\theta$  geometry using graphite monochromated Cu- $K\alpha$  X-rays ( $\lambda=1.5418 \text{ \AA}$ ), collimated on the sample in a pin-hole collimator to yield to a X-ray beam diameter of  $\sim 650 \mu\text{m}$ . The structure of the hybrid was

further analyzed by Micro-Raman spectroscopy, using a Thermo Scientific DXR with 532 nm incident photons in a range of 160-3400  $\text{cm}^{-1}$  for the large scan and 160-1100  $\text{cm}^{-1}$  for the high-resolution data. To determine the weight ratio of the composition of the hybrids, thermogravimetric analysis (TGA) was performed under air with an Auto TGA 2950 HR by TA Instruments, (5°C per minute heating rate).

A BioLogic multi potentiostats/galvanostats/EIS VPS-300 was used for electrochemical characterizations. A homemade, symmetrical two-electrode cell was used for the measurements, see Figure 5.14. Electrodes were prepared using a slurry with the active material and 1% PTFE in DI water as a binder. A stainless mesh (100 mesh size) disc with a diameter of 12 mm was used as a current collector for every electrode. When the current collector was completely covered with the slurry approximately 3 mg of active material was loaded. The electrodes were dried overnight in a vacuum oven at 40°C. As a reference, a commercially available carbon black powder (KetjenBlack, KB) was used with 60% PTFE in DI water for preparing electrodes. A Whatman GF/c glass filter was used as a separator (diameter of 16 mm, thickness of 265  $\mu\text{m}$ ). 1M  $\text{Na}_2\text{SO}_4$  in DI water was used as an electrolyte and 600  $\mu\text{l}$  of it were loaded for a cell. The cell was disassembled after electrochemical test and the material on the electrodes was dispersed in water to remove any residues including sodium salts.

Galvanostatic Charge-Discharge (GCD), Cyclic Voltammetry (CV) and Electron Impedance Spectroscopy (EIS) were performed to characterize electrochemical behavior. GCD was performed at 0.06 and 0.16 A/g with cutoff potential of  $\pm 1.5\text{V}$ . Scan rates of 0.5, 2 and 5 mV/s were used for the CV ranging from -1.5 V to +1.5 V. EIS was performed in a frequency range between 122 kHz and 100 mHz.

### 5.2.1.2 Results and Discussion

The electrode materials were synthesized by hydrothermal route in order to achieve a conductive and porous graphene-based structure. In chapter 3 has been explained the reduction process and the synthesis of graphene 3D nanostructures. The samples after the treatment looked like a black block (see Figure 3.23) in clear water with an high mechanical resistance

and the elasticity. The change of the color from brown to black it is to attribute to the reduction of the GO into reduced GO (RGO) as is shown by the XPS results. The samples kept their shape after the drying process with a very low amount of volume loss of about 30%.

The same result was obtained by performing the hydrothermal process starting from a GO/PMA/DI water dispersions. After the hydrothermal process, a similar black porous material was found in the autoclave immersed in clear water, with deposition at the bottom of the vial of a black/blue material. The morphological structure of the composite was evaluated by FESEM and TEM and in Figure 5.3 are compared with an hydrothermally prepared reduced graphene oxide sample. As clearly shown from the FESEM images, the porous structures obtained from samples of graphene only and graphene/MoO<sub>2</sub> composite are really similar, with the difference that the hybrid material shows the walls of the graphene structure completely covered by spherical nanoparticles.

The porous structure previously observed in the RGO sample was preserved, while graphene

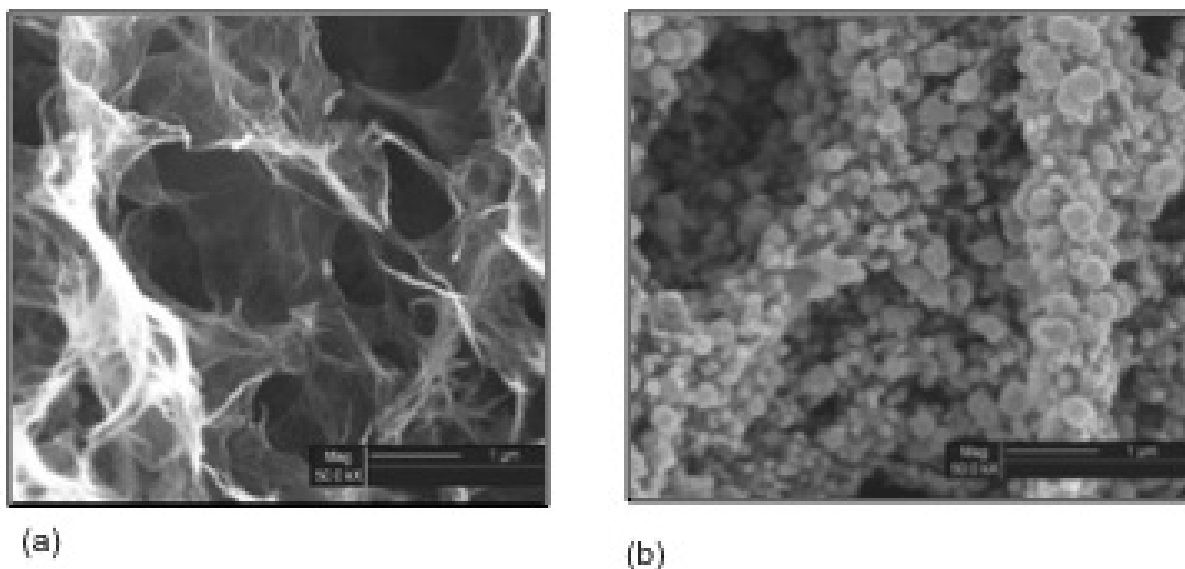


Figure 5.3 FESEM pictures of (a) RGO and (b) RGO/MoO<sub>2</sub> composite synthesized by hydrothermal process.

sheets appear decorated by oxide nanoparticles, with an average particle radius of 150 nm, as it is shown in Figure 5.4. Each particle is composed by an aggregation of nano-sized crys-

tal grains with a size of about 30 nm and it is apparent that no bare surface of graphene is observed as the nanoparticles of molybdenum oxide cover the surface uniformly. The crys-

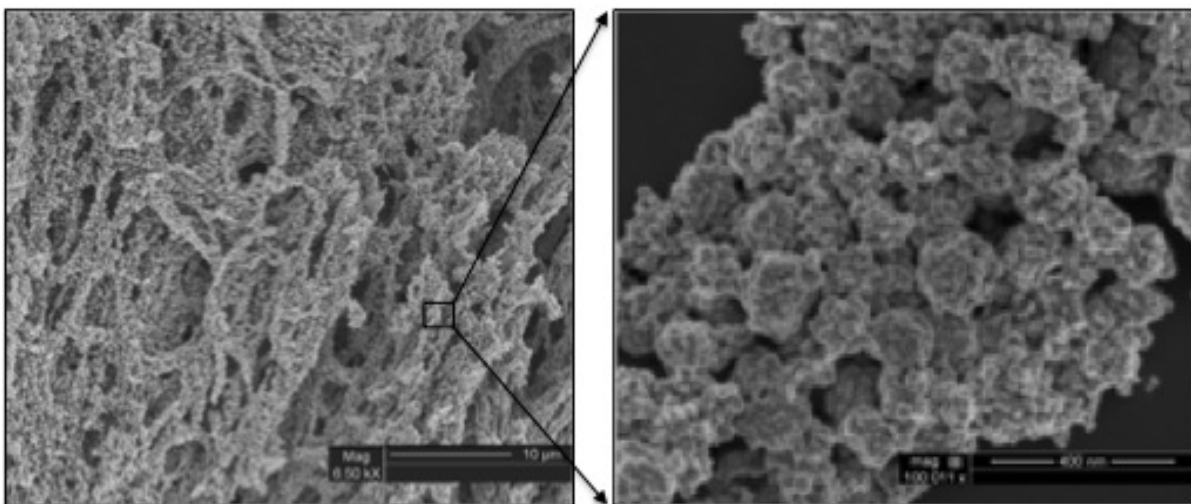


Figure 5.4 FESEM pictures of RGO/MoO<sub>2</sub> composite synthesized by hydrothermal process, showing the graphene porous structure and the presence of MoO<sub>2</sub> nanoparticles decoration.

tallinity of nanoparticles was revealed with TEM measurements, the bright field TEM image in Figure 5.5 a, shows nanoparticles of molybdenum oxide on the surface of reduced graphene oxide. In Figure 5.5 b the HRTEM picture shows the polycrystalline nature of the molybdenum oxide nanoparticles, which confirmed the presence of an ordered crystal structure. The EELS data, showed in Figure 5.6 confirmed the nature of the nanoparticles, showing the presence of molybdenum and oxygen. The polycrystalline nature of MoO<sub>2</sub> nanoparticles created with similar procedure, was confirmed in the literature by selected area electron diffraction (SAED) patterns that consist of concentric rings (171).

Concerning the mechanism of the reaction occurred during hydrothermal synthesis, it is hypothesized that the synergetic effect played by the ethanol present in the PMA solution, together with the GO reduction process can be catalytic agents for the formation of MoO<sub>x</sub> nanoparticles, as previously reported in the literature (191). In fact, the synthesis of MoO<sub>x</sub> nanoparticles through hydrothermal process (178)-(181) employing ethylene glycol as reducing

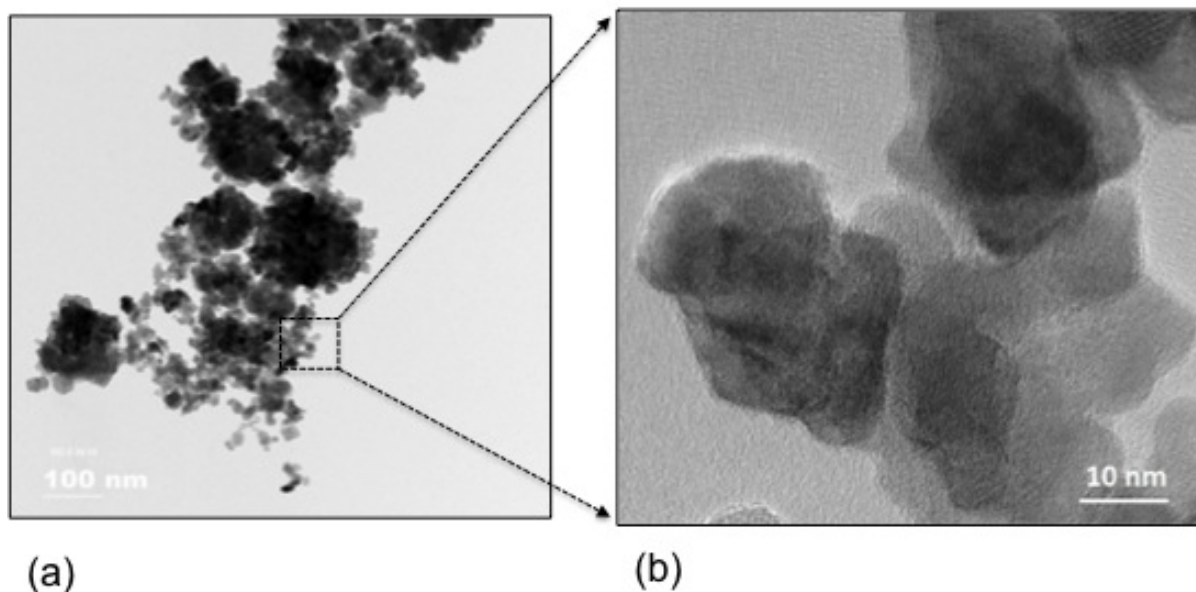


Figure 5.5 Bright-Field TEM images of MoO<sub>2</sub> nanoparticles (a) and HRTEM magnification of crystalline structure (b).

agent and graphite oxide/MoO<sub>2</sub> composites has been extensively studied for Li-ion batteries, using different precursors and procedures (166)-(179). A confirmation of the fact that the hydrothermal process altered the PMA to form molybdenum oxide on the graphene structure came from the XPS analysis, which revealed the presence of Mo in the survey spectra, as reported in Figure 5.7.

The formation of molybdenum oxide from PMA during the hydrothermal synthesis is further confirmed by XPS results in Figure 5.8. The presence of Mo is supported by the survey spectrum and deconvolution of peaks of Mo 3d and C1s. The reduction of the graphene oxide by using the hydrothermal synthesis also in the presence of PMA was confirmed by analyzing the C1s peak, that shows a strong decrease in the intensities of peaks related to oxygen functionalities C-O at 286.3 eV and C=O at 287.6 eV and the complete disappearance of the O-C=O peak as compared to the peaks of graphene oxide samples presented in Chapter 3 (111), (94) and (183). The analysis of the deconvolution peak of the Mo 3d, reported in Figure 5.8, shows how the intensities for the 3d<sub>5/2</sub> peaks are lower compare to the Mo 3d<sub>3/2</sub> ones (184). Mo 3d<sub>5/2</sub> peak is located at 229.6 eV and the Mo 3d<sub>3/2</sub> peak at 232.8 eV, with a characteristic difference

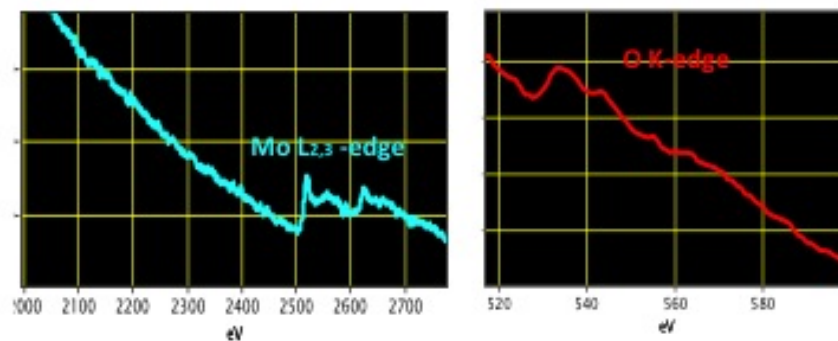


Figure 5.6 Electron Energy loss spectra performed on the nanoparticles.

of binding energy of 3.2 eV (185), (186). This doublet characteristic suggests the presence of Mo (IV) oxidation state as MoO<sub>2</sub> (187). The doublet at 232.3 eV for Mo (VI) 3d<sub>5/2</sub> and at 235.6 eV for Mo (VI) 3d<sub>3/2</sub> can be addressed to the possible surface oxidation of the MoO<sub>2</sub> in air as reported previously (188), (189).

The crystalline phase of MoO<sub>2</sub> nanoparticles was confirmed by XRD as presented in Figure 5.9. The x-ray diffractogram indicates the presence of monoclinic MoO<sub>2</sub> phase with a disordered rutile structure (172).

In particular, XRD spectrum in Figure 5.9 a represents the MoO<sub>2</sub> nanoparticles deposited at the bottom of the autoclave at the end of the hydrothermal synthesis, while in Figure 5.9 b is reported the spectrum of the RGO/MoO<sub>2</sub> composite. The RGO/MoO<sub>2</sub> composite spectrum shows the contribution of the RGO peak around 18.3 degree, confirming the presence of carbon (see chapter 3, Figure 3.26), together with the diffraction peaks indexed to MoO<sub>2</sub> monoclinic phase.

The structure of the nanocomposites was analyzed by Micro-Raman spectroscopy and in Figure 5.10 a, is reported a comparison of Raman spectra of RGO starting material, MoO<sub>2</sub> nanoparticles and the RGO/MoO<sub>2</sub> composite. The RGO spectrum shows the D, G and 2D bands respectively centered at 1345, 1595 and 2694 cm<sup>-1</sup> typical of nanostructured graphitic carbon (190). The D band presents a higher intensity than the G band, which identifies a substantial degree of disorder due to structural defects at the surface and edges of RGO flakes. MoO<sub>2</sub> nanoparticles presents the peaks at 284, 337, 376, 663, 820 and 993 cm<sup>-1</sup> typical of monoclinic

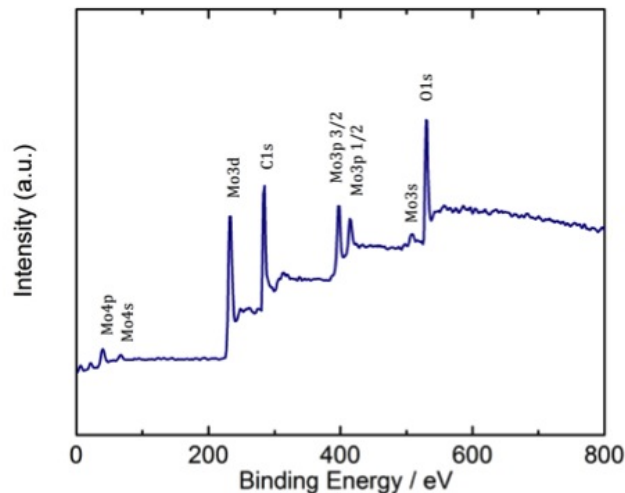


Figure 5.7 XPS survey spectra of the rGO/MoO<sub>2</sub> composite.

MoO<sub>2</sub> (192). The RGO/MoO<sub>2</sub> composite presents peaks relative to both materials. Figure 5.10 b reports a zoom at low wavenumbers confirming the presence of MoO<sub>2</sub> in the composite.

The weight ratios between MoO<sub>2</sub> nanoparticles and RGO in the composite was investigated by TGA in air. Figure 5.11 shows the weight loss percentage plotted against temperature for RGO, MoO<sub>2</sub> nanoparticles, and the RGO/MoO<sub>2</sub> composite samples. RGO presents a sharp weight drop above 400°C, while MoO<sub>2</sub> nanoparticles show an oxidation process with phase change to MoO<sub>3</sub> starting around 320°C. A similar phase change from MoO<sub>2</sub> to MoO<sub>3</sub> is observed for RGO/MoO<sub>2</sub> composite, with a weight increase around 350°C, and a sudden weight drop after 400°C due to degradation of carbon species, to final stabilization in a plateau after 500°C (191). Comparing the residual weight measured at this plateau with the values measured for MoO<sub>2</sub> nanoparticles, the percentage of graphene with respect to MoO<sub>2</sub> in the composite was calculated to 28.2%.

To confirm the change of phase of the nanoparticles observed during TGA, XRD characterization was performed on a composite sample after heating in oven for two hours at 325°C Figure 5.12. This temperature was chosen in order to achieve the change of phase of the nanoparticles without completely losing the RGO content. The characteristic peaks of the orthorhombic

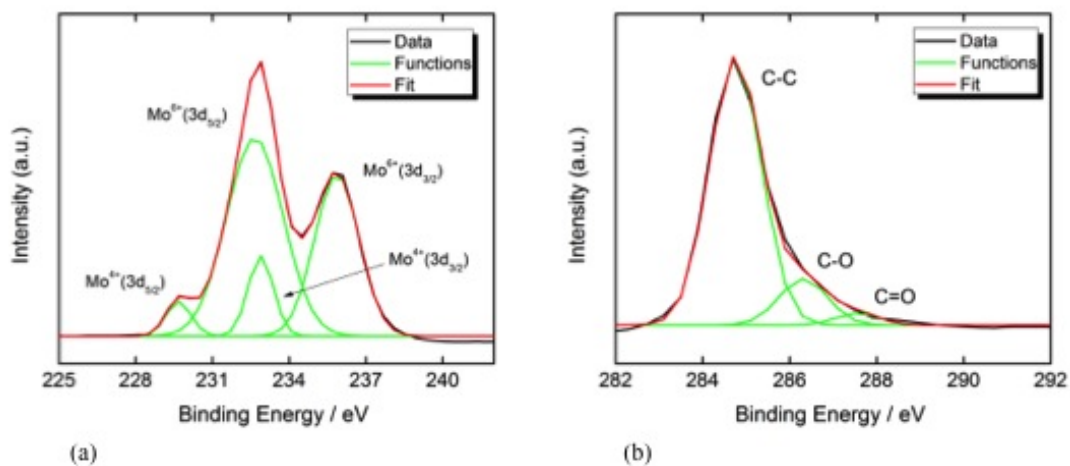


Figure 5.8 XPS deconvolution spectra of (a) the C1s peak and (b) the Mo 3d high-resolution scans.

MoO<sub>3</sub> phase are clearly revealed , moreover a color change from dark blue (RGO/MoO<sub>2</sub>) to gray (RGO/MoO<sub>3</sub>) is clearly visible after the annealing, see Figure 5.13 (175).

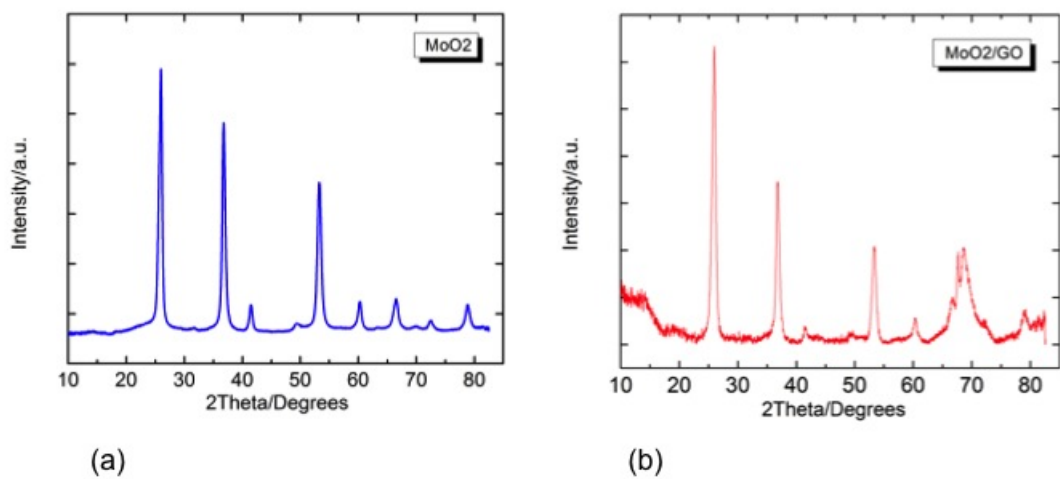


Figure 5.9 XRD spectra of MoO<sub>2</sub> nanoparticles.

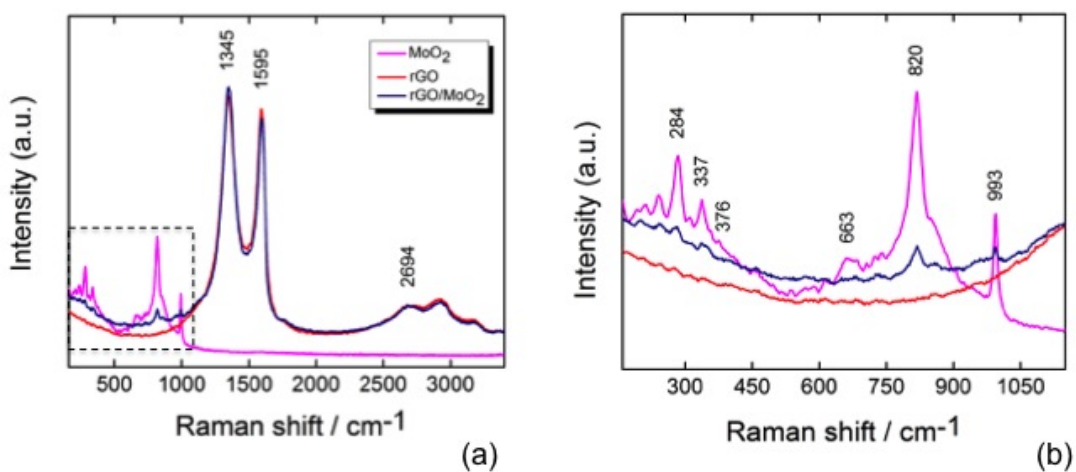


Figure 5.10 Micro-Raman spectra of RGO, MoO<sub>2</sub> nanoparticles and the RGO/MoO<sub>2</sub> composite.

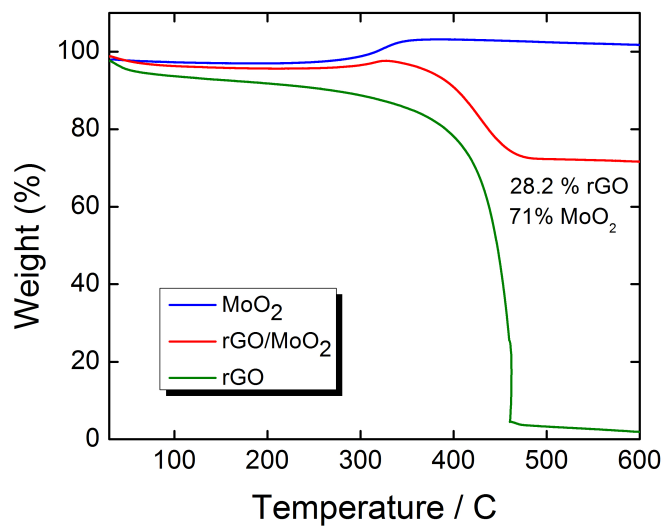


Figure 5.11 TGA of RGO (green), MoO<sub>2</sub> nanoparticles (blue) and RGO/MoO<sub>2</sub> composite (red).

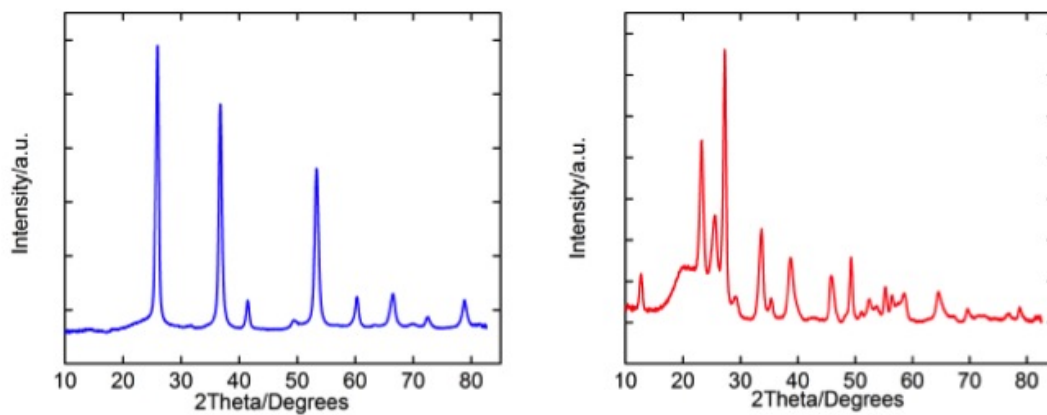


Figure 5.12 XRD spectra of MoO<sub>2</sub> nanoparticles before (blue graph) and after the TGA (red graph).

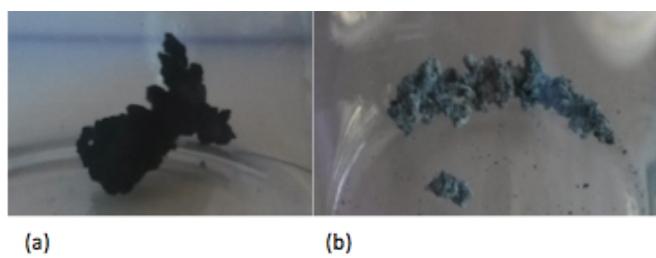


Figure 5.13 Photograph of the RGO/MoO<sub>2</sub> composite before (a) and after (b) annealing at 325°C.

The electrochemical performance, like the specific capacitance, the equivalent series resistance and the ion intercalation respect to the RGO/MoO<sub>2</sub> electrodes were assessed by cyclic voltammetry (CV), electrochemical impedance spectroscopy (EIS) and galvanostatic charge discharge (GCD) respectively. The electrolyte used for the electrochemical characterization was aqueous-based. The electrochemical properties were compared with RGO and KJ Black electrodes.

A symmetric electrochemical cell configuration was used for the electrochemical characterization, see Figure 5.14, a Whatman GF/c glass fiber separator with a diameter of 16 mm and a thickness of 265  $\mu\text{m}$  was used as separator, 600  $\mu\text{l}$  of 1M Na<sub>2</sub>SO<sub>4</sub> in DI water was used as electrolyte and stain less steel metal grids were used as current collectors. GCD was performed

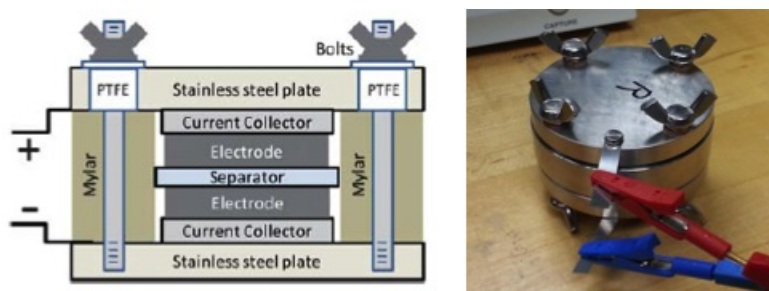


Figure 5.14 Photograph of the two-electrode cell used for the electrochemical characterization.

at 0.06 and 0.16 A/g limiting the potential at +1.5V and -1.5 V. The scan rates used for the CV curves were 0.5, 2 and 5 mV/s in a potential range between -1.5 V and +1.5 V. EIS was performed in a frequency range between 100 mHz and 122 kHz. The specific capacitances were calculated based on the mass of the active material.

Electrodes of only KB or RGO were tested for the comparison. Figure 5.15 shows charge/discharge profiles of three different electrodes. Both KB and RGO show rapid potential changes during charge (or discharge) process, which indicates rapid polarization of the electrodes. Interestingly, the hybrid electrode shows very stable plateau at 0.9V during charge (or discharge). This implies that the MoO<sub>2</sub> of the hybrid facilitates the insertion of ions in the electrolyte rather than simple polarization of the electrode. Similar to the previous work on lithium ion insertion to the MoO<sub>2</sub>, which is associated with the monoclinicorthorhombicmonoclinic phase transition,

this charge/discharge behavior suggests the insertion of sodium cations into the  $\text{MoO}_2$  on the hybrid electrode (166).

In the characteristics of KJ Black and RGO electrodes, obtained using the same experimental

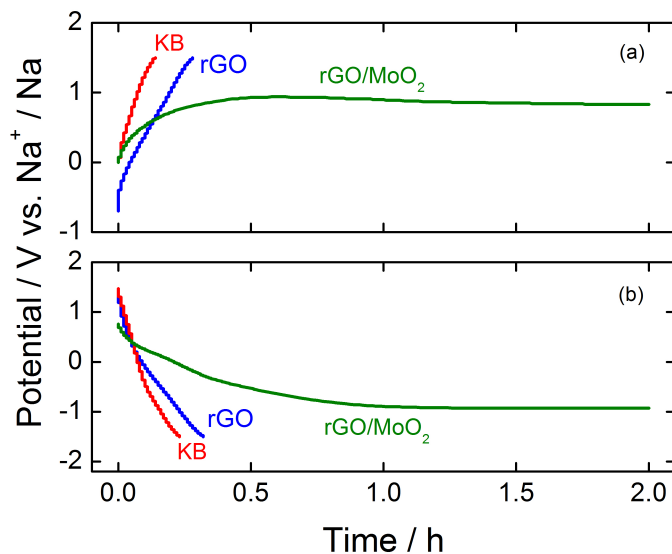


Figure 5.15 GCD profiles of RGO/MoO<sub>2</sub>, KJ Black and RGO electrodes recorded in the range of -1.5 V to 1.5 V, at a current of 0.5 mA at 1 mAh.

parameters and conditions, this plateau was not measured, as expected in absence of Na ions intercalation. Galvanostatic discharge profiles of up to 4 cycles are shown in Figure 5.16. A discharge profile with RGO electrode is also shown for comparison. It is noted that the first discharge profile of the hybrid electrode is very different from the rest of cycles. A potential plateau of -0.75V is clearly observed along with large capacity compare to the rest of cycles. This plateau is very likely due to the transition from  $\text{MoO}_2$  to  $\text{Na}_x\text{MoO}_2$ , which is induced by the insertion of  $\text{Na}^+$  ions to the hybrid electrode during discharge process. A rapid potential drop was observed after capacity of 300 mAh/g, which leads to the failure of the cell. Though the capacity of the hybrid electrode after the first cycle (2nd to 4th cycles) is higher than that of RGO electrode, no potential plateau is observed. This implies the existence of non-reversible electrochemical reaction during the very first cycle of the galvanic discharge. This might be due to the formation of an SEI layer on the surface of the electrode similar to the lithium ion battery electrodes (166), (196).

The cyclic voltammograms (CV) in Figure 5.17 further confirm the redox reactions on the hy-

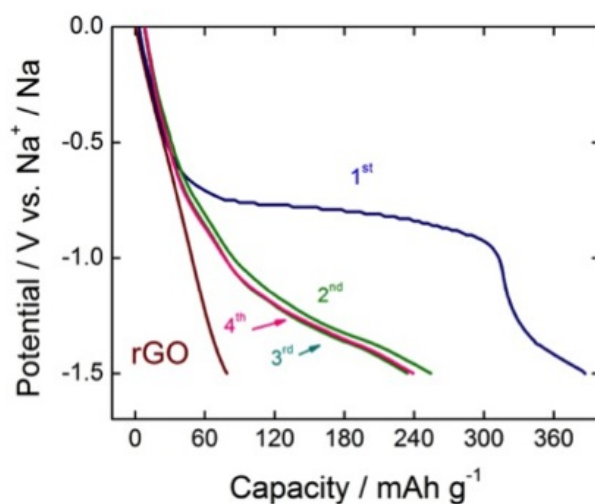


Figure 5.16 Galvanostatic discharges of RGO/MoO<sub>2</sub> and RGO electrodes at a current of 0.5 mA at 1 mAh, first four cycles.

brid electrode. With the scan rate of 0.5 mV/s, clear reduction/oxidation peaks around -1.0V and +1.0V were observed. The origin of the secondary redox peaks at  $\pm 0.4$ V, which become more evident at higher scan rates is unclear at the moment, in fact from the second cycle and for faster scan rates, two distinct and highly reversible redox couples at 0.9 V and 0.4 V can be observed Figure 5.18, which can be related to the phase transition process from MoO<sub>2</sub> to Na<sub>x</sub>MoO<sub>2</sub>, due to partial and gradual Na ion insertion into the electrode (179). Figure 5.19 shows the sixth CV cycles at 0.5 mV/s of RGO and RGO/MoO<sub>2</sub>. The differences of the CV curves such as amplitude of the hysteresis loop and existence of redox peaks, confirm the nature of double layer capacitor of the RGO compared to the pseudocapacitor behavior brought by metal oxides. As shown from the values of specific capacitance reported in Table 5.1, this behavior results in three times higher capacity of the hybrid compared to the RGO (381 vs. 140 F/g). This indicates that the ion insertion to the MoO<sub>2</sub> electrodes contributes to increase the specific capacitance of the supercapacitor.

The specific capacitance of the supercapacitor with composite electrodes was extrapolated from CV measurements. A comparison of the capacitance values at 0.5 mV/s, 2 mV/s and 5 mV/s

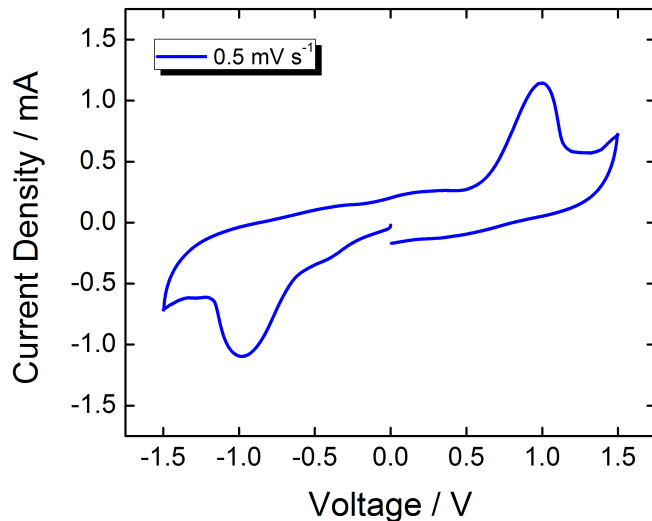


Figure 5.17 First CV cycle of RGO/MoO<sub>2</sub> electrodes recorded in the range of -1.5V to 1.5V, with a scan rate of 0.5 mV/s.

scan rate for the RGO/MoO<sub>2</sub> and the RGO electrodes are reported in Table 5.1, calculated from the CV curves of a two-electrode electrochemical cell using the following relationships (197):

$$C_{Sp}(Fg^{-1}) = 4 \frac{C}{m}$$

with

$$C = \frac{I}{\frac{dV}{dt}}$$

where  $C_{sp}$  is the specific capacitance calculated on the mass of active material for each electrode,  $C$  is the capacitance calculated from the CV curves,  $I$  is the measured current calculated as integral of the discharging curve and  $dV/dt$  is the scan rate. A significant increase of

Table 5.1 Specific capacitances of RGO and RGO/MoO<sub>2</sub> electrodes at 0.5, 2 and 5 mV/s scan rates calculated from CV measurements.

Scan rate (mV/s)	rGO Sp Capacitance (F/g)	rGO/MoO <sub>2</sub> Sp Capacitance (F/g)
0.5	140.18	381.1
2	100.35	206.4
5	67.63	143.34

the specific capacitance for the composite electrodes respect to RGO electrodes occurred at 0.5

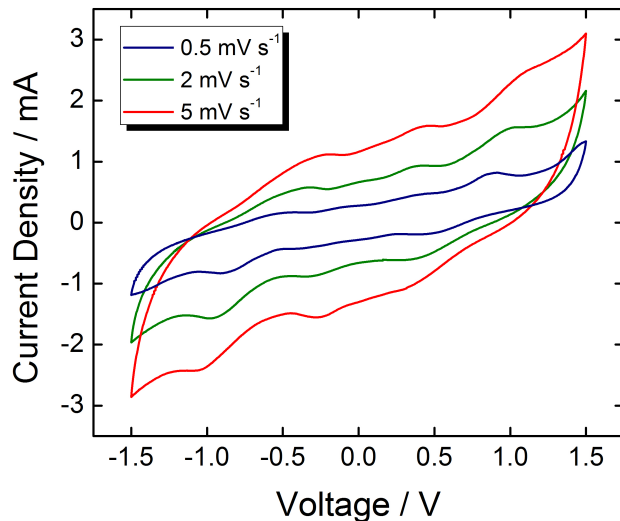


Figure 5.18 CV profiles of the current density versus voltage of RGO/MoO<sub>2</sub> electrodes recorded in the range -1.5V to 1.5V, with a scan rate of 0.5, 2 and 5 mV/s.

mV/s scan rate, while as expected for higher scan rates the calculated values of capacitance are similar for both types of electrode, confirming the contribution due to the pseudocapacitance and the intercalation of Na ions into the MoO<sub>2</sub> nanoparticles network.

The synergistic effect between RGO and MoO<sub>2</sub> nanoparticles in the composite electrodes is beneficial to the capacitance of the devices, as the flexible structure of RGO helps absorbing the volume change of MoO<sub>2</sub> during intercalation, while at the same time the presence of MoO<sub>2</sub> nanoparticles prevents RGO from restacking. When used together in a composite, these materials form a highly conductive and flexible network allowing improvement of cycling stability, energy and power densities compared to other types of supercapacitors like the EDLC. The structural and compositional changes in the MoO<sub>2</sub> nanocrystals were assessed using HRTEM, EDS and XRD. The results are shown in Figure 5.20 a, Figure 5.20 b and Figure 5.20 c, respectively. As shown in Figure 5.20 b, Na k edge peak was observed from the hybrid after insertion of sodium ion. However, no clear evidence of structural changes in crystal phase of MoO<sub>2</sub> was observed. The XRD diffractograms of MoO<sub>2</sub> crystal phase before and after ion insertion are identical indicating no phase transition by the ion insertion. The equivalent series resistance determined by EIS measurement suggests that the MoO<sub>2</sub> in the hybrid lowers the impedance

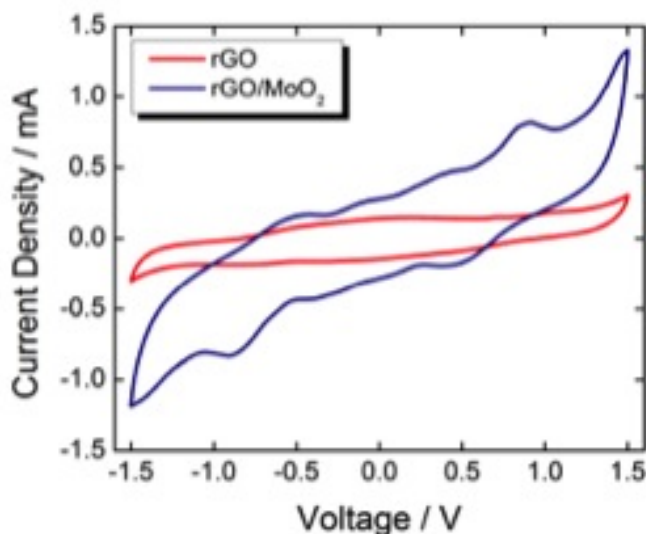


Figure 5.19 CV profiles of the current density of RGO (red line) and RGO/MoO<sub>2</sub> (blue line) electrodes versus voltage in the range -1.5V to 1.5V, with a scan rate of 0.5, mV/s.

of the cell. This might be due to the lower conductivity of the hybrid by containing packed metal oxide nanoparticles. EIS was performed on the RGO/MoO<sub>2</sub> electrodes, and for reference also on RGO electrodes as shown in Figure 5.21. From this measurement, the Equivalent Series Resistance (ESR) can be calculated as the intersection between the curve of the Nyquist plot and the X-axis (197). The ESR is defined as a combination of the electronic resistance of the electrode material, the interface resistance between the electrode and the current collector, the ionic diffusion resistance of ions moving in the small pores of the electrode and through the separator, and the electrolyte resistance. In order to accurately calculate the values of ESR, the equivalent electric circuits describing double-layer capacitance and pseudocapacitance reported in Figure 5.22 were used (198), (199).

The group formed by  $R_1$ ,  $R_2$  and  $C_1$  represents the ESR, the  $C_2$  with  $R_3$  corresponds to the double-layer capacitance contribution, while the  $R_4$  with  $C_3$  represents the pseudocapacitance contribution. The zFit BioLogic (ECLab) software was then used to calculate the fitting curves of the EIS data previously collected. The experimental data points and the fitting curves are reported in Figure 5.21, where the double-layer equivalent electric circuit was applied to KJB and RGO data, while the complete model (EDCL and pseudocapacitance) was used to fit the

RGO/MoO<sub>2</sub> data. The ESR calculated by the software are reported in Table 5.2, together with the values calculated from the constant current (CC) curve using the IR drop at the beginning of the discharge (197).

The conductivity of the RGO of 1 mS/cm estimate by the EIS impedance measurement ob-

Table 5.2 Comparison of ESR values for RGO, KJB and RGO/MoO<sub>2</sub> electrodes calculated from GCD measurements (IR drop of the discharge using CC curves) and from zFit software fitting of EIS data.

<b>Sample</b>	<b>ESR GCD (Ohm)</b>	<b>ESR zFit (Ohm)</b>
rGO	240 ± 5	258 ± 5
rGO/MoO <sub>2</sub>	118 ± 5	141 ± 5

tained with a two electrode cell that showed an estimate resistance of 240 Ohm. As expected, the ESR of the RGO/MoO<sub>2</sub> composite electrodes is lower than the values of the RGO electrode, due to the contribution to conductivity given by MoO<sub>2</sub> nanoparticles, which play a role of connector between graphene sheets allowing longer paths for electron drift.

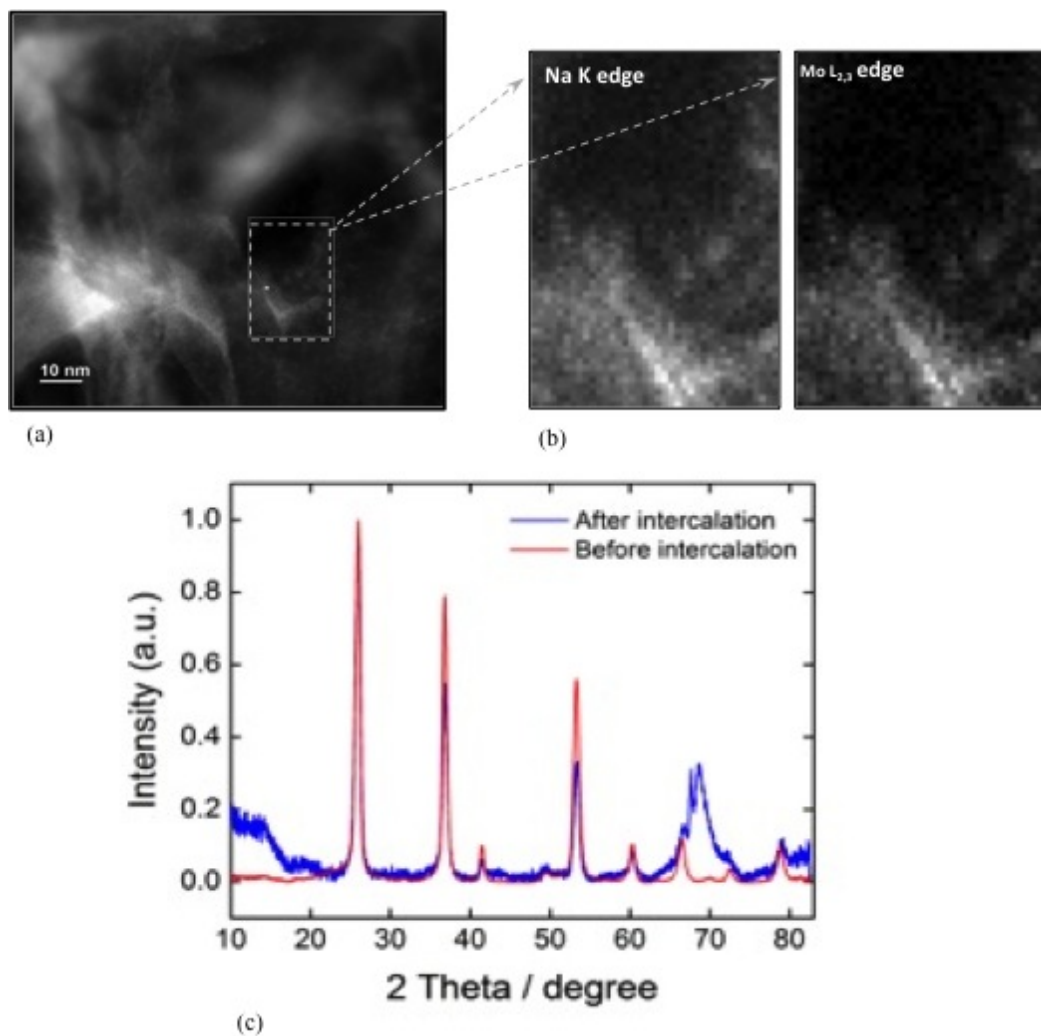


Figure 5.20 FESEM picture of the RGO/MoO<sub>2</sub> electrodes after discharge (a), EDS mapping of Na k and Mo L edges (b) and XRD spectra before and after (blue) discharge process (c).

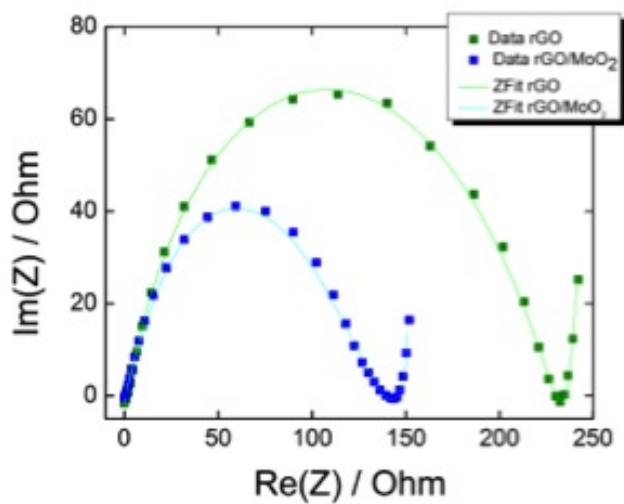


Figure 5.21 EIS after 5 GCD cycle of RGO (green line) and RGO/MoO<sub>2</sub> (blue line) electrodes.

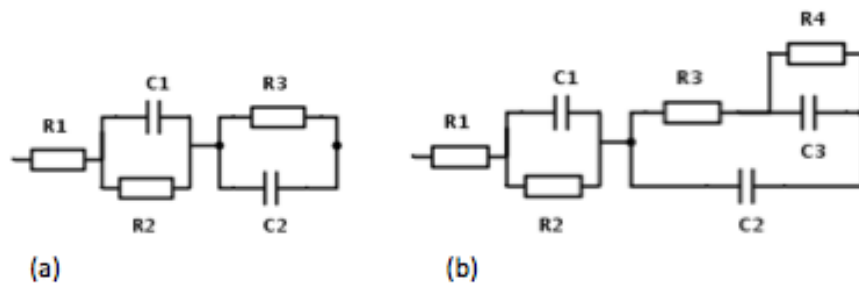


Figure 5.22 Equivalent electric circuit of a double-layer capacitor used for RGO and KJB electrodes (a) and of a pseudocapacitor used for RGO/MoO<sub>2</sub> electrode (b).

## 5.2.2 Other Graphene Composites

In the next section the synthesis methods and the characterizations of other type material composites with the graphene, are reported and discussed. Three different composites are going to be presented: first will be reported a graphene/titanium dioxide composite obtained with hydrothermal synthesis, very similar to the graphene/molybdenum dioxide process but with lower values of specific capacitance, then the synthesis of a graphene/expanded graphite composite, pursuing the goal of obtaining the same electrode performance of the graphene based electrodes but lowering the cost for the material by reducing the amount of graphene. In the end, a composite of graphene and sodium silicate gel will be presented through an in situ synthesis of the electrode material and the reduction of the graphene oxide in the alkaline environment.

### 5.2.2.1 Hydrothermal Synthesis of rGO/Titanium Dioxide Composites

Self assembled structure of graphene oxide and  $\text{TiO}_2$  have been reported in literature (200), and their application as electrode material for lithium ion batteries has also been proved (201). The use of sodium ion as intercalating material for new generation sodium ion batteries has been recently proposed for rutile phase  $\text{TiO}_2$  (202) and in 2014 a proof of the possible intercalation of sodium ion in the anatase phase has also been proposed (203). In the experiment proposed in the next paragraphs will be investigated the possibility of intercalate the sodium ions in the crystalline structure of the  $\text{TiO}_2$  anatase phase and will be tried to achieve high specific capacitance values for supercapacitor applications.

**Materials and Methods** Nanoparticles of titanium oxide P25 were purchased from VP Aeroperl Degussa, graphene oxide (thickness 0.7-1.2 nm) was purchased from ACS Materials (USA), poly(tetrafluoroethylene) (PTFE), and  $\text{Na}_2\text{SO}_4$  were purchased from Sigma-Aldrich. Deionized (DI) water was used as a solvent for the electrolyte. The samples were prepared starting from a dispersion of GO in water sonicated in a bath sonicator for about 15 minutes. When big particles were no longer visible the titanium dioxide powder was added to the disper-

sion and sonicated again for 15 minutes. The ratios of GO/TiO<sub>2</sub> prepared were 5:1, 1:4, 1:3 and 1:1. The resulting dispersion was then transferred in a Teflon lined stain less steel autoclave of 25 ml total volume and put in the vacuum oven at the temperature of 180°C degree for 16 hours.

In order to perform the characterizations all the samples after the synthesis were freeze dry overnight. For the electrochemical measurements electrodes were assembled preparing slurry with the active material and 1% PTFE in DI water as a binder. A stainless mesh (100 mesh size) disc with a diameter of 12 mm was used as a current collector. When the current collector was completely covered with the slurry approximately 3 mg of active material was loaded. The electrodes were dried overnight in a vacuum oven at 40°C. A two electrode cell was used for the electrochemical characterizations and a Whatman GF/c glass filter was used as a separator (diameter of 16 mm, thickness of 265 μm). 1M Na<sub>2</sub>SO<sub>4</sub> in DI water was used as an electrolyte and 600 μl were loaded in the cell.

**Results and Discussion** As already presented and discussed in the previous section, through a simple hydrothermal synthesis it is possible to obtain 3D nanostructures made of graphene and decorated by metal oxide nanoparticles. From the initial dispersion of GO/TiO<sub>2</sub> nanoparticles in water (thick beige solution), it was obtained a black block at the bottom of the autoclave immersed in clear water. Graphene oxide and TiO<sub>2</sub> have been mixed in different ratios in order to obtain different morphologies, that are presented in Figure 5.23, where respectively are shown the 5:1, 1:1, 1:3 and 1:4 ratio between GO and TiO<sub>2</sub>.

For what concerns the ratio 5:1, it is noticeable that the structure of the graphene creates pores with different diameters resulting in an intricate structure slightly decorated by some aggregation of TiO<sub>2</sub> nanoparticles in random positions without reaching a uniform coverage of the walls. For the samples with GO/TiO<sub>2</sub> ratio of 1:4 and 1:3, it is possible to notice a larger amount of TiO<sub>2</sub> nanoparticles that cover completely the 3D graphene structure forming even cluster of nanoparticles due to the high concentration. For this reason the amount of P25 was considered too high, because beside achieve a very good and homogenous coverage of the

sample, big cluster of P25 were observed in all the samples. The best solution was obtained using a ratio of 1:1, showed the FE-SEM pictures in Figure 5.23 b, assures a good coverage of the GO porous structure avoiding the aggregation of nanoparticles in big clusters and the subsequent obstruction of the pores.

To confirm the nature of the materials obtained and to assure that the crystalline phase of the  $\text{TiO}_2$  wasn't change in the synthesis process, Raman spectroscopy analysis was performed. In Figure 5.24 are reported the Raman data obtained on a 1:1 sample, and it is possible to deduce that the initial graphene oxide has been reduced as expected if compare di different intensities of the D and G peaks and confirms the presence of  $\text{TiO}_2$ . The intensity of the D peak of the carbon is higher than the G peak that is a sign of the reduction of the graphene oxide and the increase of the disorder degree, explained in chapter 3, see Figure 3.27. The analysis of the  $\text{TiO}_2$  peaks confirms the presence of anatase phase (203) and the fact that the hydrothermal synthesis does not affect the crystalline nature of the material.

Electrochemical measurement have been performed using  $\text{GO}/\text{TiO}_2$  composite as electrode material. In Figure 5.25 and Figure 5.26 are reported the cyclic voltammetry curves obtained using two different samples: the 1:1 and the 1:3 ratio at 0.5, 2 and 5 mV/s in a voltage range of +1.5 to -1.5 V. It is possible to notice as the different amount of  $\text{TiO}_2$  can give different shape in the curves and in particular introducing red/ox reactions related to the peak at  $\pm 0.4$  V and  $\pm 0.6$  V, as already discussed for the  $\text{MoO}_2$ . These peaks can be related to the intercalation processes in the crystalline structure of the sodium ions present in the electrolyte.

In Figure 5.27 are reported the electron impedance spectroscopy measurements performed on two different samples: 1:1 and 1:3 ratio. As it is possible to notice the equivalent series resistance appears to be higher for the sample with an higher amount of  $\text{TiO}_2$ , probably due to an increase of the oxide layer that lower the overall conductivity of the electrode. Finally, in Table 5.3 are reported the values calculated concerning the specific capacitance of the samples with ratio 1:1 and the RGO only. The values appear to be lower for the composite with the  $\text{TiO}_2$  compare to the pure graphene and this fact can be explained by an overall lower surface area value due to the nanoparticles occupying most of the space in the pores of the graphene structure. For this reason the composite  $\text{RGO}/\text{MoO}_2$  have been preferred as possible material

Table 5.3 Specific capacitances of RGO and RGO/TiO<sub>2</sub> (1:1) electrodes at 0.5, 2 and 5 mV/s scan rates calculated from CV measurements.

Scan rate (mV/s)	RGO Sp Capacitance (F/g)	RGO/TiO <sub>2</sub> Sp Capacitance (F/g)
0.5	140.18	90.62
2	100.35	77.38
5	67.63	68.45

for supercapacitor electrode application.

### 5.2.2.2 Hydrothermal Synthesis of rGO/Expanded Graphite Composites

The production cost of the graphene it is still considered very high and strategies to lower the global cost of the final device are largely investigated. For this reasons one of the composite investigated as possible electrode material for supercapacitor application is a combination of graphene oxide and expanded graphite. In this case, the amount of the graphene is reduced and in percentage substitute by the graphite that is cheaper on the market. In the next section will be discussed the synthesis of composites with different percentage of expanded graphite respect to the graphene and some preliminary results of specific capacitance values are reported and discussed.

**Materials and Methods** The expanded graphite was purchased from Asbury carbon and the graphene oxide was purchased from ACS Materials (USA), poly(tetrafluoroethylene) (PTFE), and Na<sub>2</sub>SO<sub>4</sub> were purchased from Sigma-Aldrich. Deionized (DI) water was used as a solvent for the electrolyte. Different percentages of expanded graphite at the 10% , 20%, 30%, 50%, and 100% compared to the total carbon amount were prepared. The samples were prepared by adding the amount of EXG in 12 ml of DI water and sonicate with a Branson 250W horn sonicator at 45% amplitude for 90 seconds with a stop of 10 seconds and go of 15 seconds in order to exfoliate the big flakes and obtaining a more uniform dispersion. It was then added to the dispersion the amount of GO and sonicate in a bath sonicator for about 15 minutes. The dispersion was then tranferred in a Teflon lined stain less steel autoclave of 25 ml total volume and put in the vacuum oven at the temperature of 180°C degree for 16 hours. In order to complete the characterizations all the samples after the synthesis were freeze dry

overnight.

In order to perform the characterizations all the samples after the synthesis were freeze dry overnight. For the electrochemical measurements electrodes were assembled preparing a slurry with the active material and 1% PTFE in DI water as a binder. A stainless mesh (100 mesh size) disc with a diameter of 12 mm was used as a current collector. When the current collector was completely covered with the slurry approximately 3 mg of active material was loaded. The electrodes were dried overnight in a vacuum oven at 40°C. A two electrode cell was used for the electrochemical characterizations and a Whatman GF/c glass filter was used as a separator (diameter of 16 mm, thickness of 265  $\mu\text{m}$ ). 1M  $\text{Na}_2\text{SO}_4$  in DI water was used as an electrolyte and 600  $\mu\text{l}$  were loaded in the cell.

**Results and Discussion** The samples were prepared decreasing the amount of GO and substituting it with surface enhanced graphite called also expanded graphite (EXG), this material has been introduced and discussed in Chapter 2, where it was employed as starting material for the graphene synthesis methods. Samples with different percentages of the graphite amount have been prepared and in Figure 5.28 are compared respectively the 10% and the 50% samples.

The sample with only the 10% of expanded graphite looks very similar to the 100% graphene oxide samples (see Figure 3.26), the color of the resulting material is black and with a good elasticity and resistance to the pressure stress. In Figure 5.28 b is showed a picture of the 50% expanded graphite sample and it is possible to notice the typical gray color of the graphite due to the higher concentration of it. Not only the color changed, but also the elasticity properties are lost and it results in an increase of the fragility, due to the different bonding generated by the hydrothermal synthesis. In fact, the expanded graphite does not go through a reduction process as happens to the graphene oxide and for this reason, no strong interaction are generated by the graphite itself.

As is possible to see from the FE-SEM picture in Figure 5.28 c and d the more is increasing the amount of EXG the more is lost the porous structure due to the GO with its effect of binder due to the forces generated during the hydrothermal synthesis and it is going toward a more

aggregation of flakes with a lower mechanical resistance. The two samples are compared with the same magnifications in Figure 5.29 and in fact, the sample with 10% presents a sporadic amount of graphite flakes and that are completely embedded in the graphene structure, on the contrary, the 50% sample shows a very low amount of graphene flakes. A necessary adjustment of the EXP amount, in order to maximize the percentage of expanded graphite without losing completely the benefic effect of the graphene oxide in terms of surface area and elasticity was needed and the best solution has been obtained by using the 30% of expanded graphite respect to the total amount of carbon material. In Figure 5.30 are reported FE-SEM pictures at different magnifications of the sample, and it is possible to notice that if compared to the 10% and 50% samples, the porous structure of the 30% sample is more equilibrate; the graphite is present in a no negligible amount and the graphene oxide forms a self sustaining structure, that give the support to the overall shape.

Electrochemical measurements have been also performed on the optimized material and the resulting curves of the cyclic voltammetry analysis are reported in Figure 5.31. The electrodes were run at 0.5, 2 and 5 mV/s in a voltage range of 1.5 to -1.5 V and the specific capacitance values reported in Table 5.4 were calculated with the standard formula reported previously in this chapter.

The values of the specific capacitance for the composite are surprisingly very similar to the

Table 5.4 Specific capacitances of RGO and 30% expanded graphite/rGO electrodes at 0.5, 2 and 5 mV/s scan rates calculated from CV measurements.

Scan rate (mV/s)	rGO Sp Capacitance (F/g)	rGO/MoO <sub>2</sub> Sp Capacitance (F/g)
0.5	140.18	135.83
2	100.35	104.68
5	67.63	88.84

sample with 100% graphene oxide and for higher scan rates the composite has even a slightly higher specific capacitance. This result seems to be a promising possibility to lower the materials cost for the production of electrodes for EDLC supercapacitors.

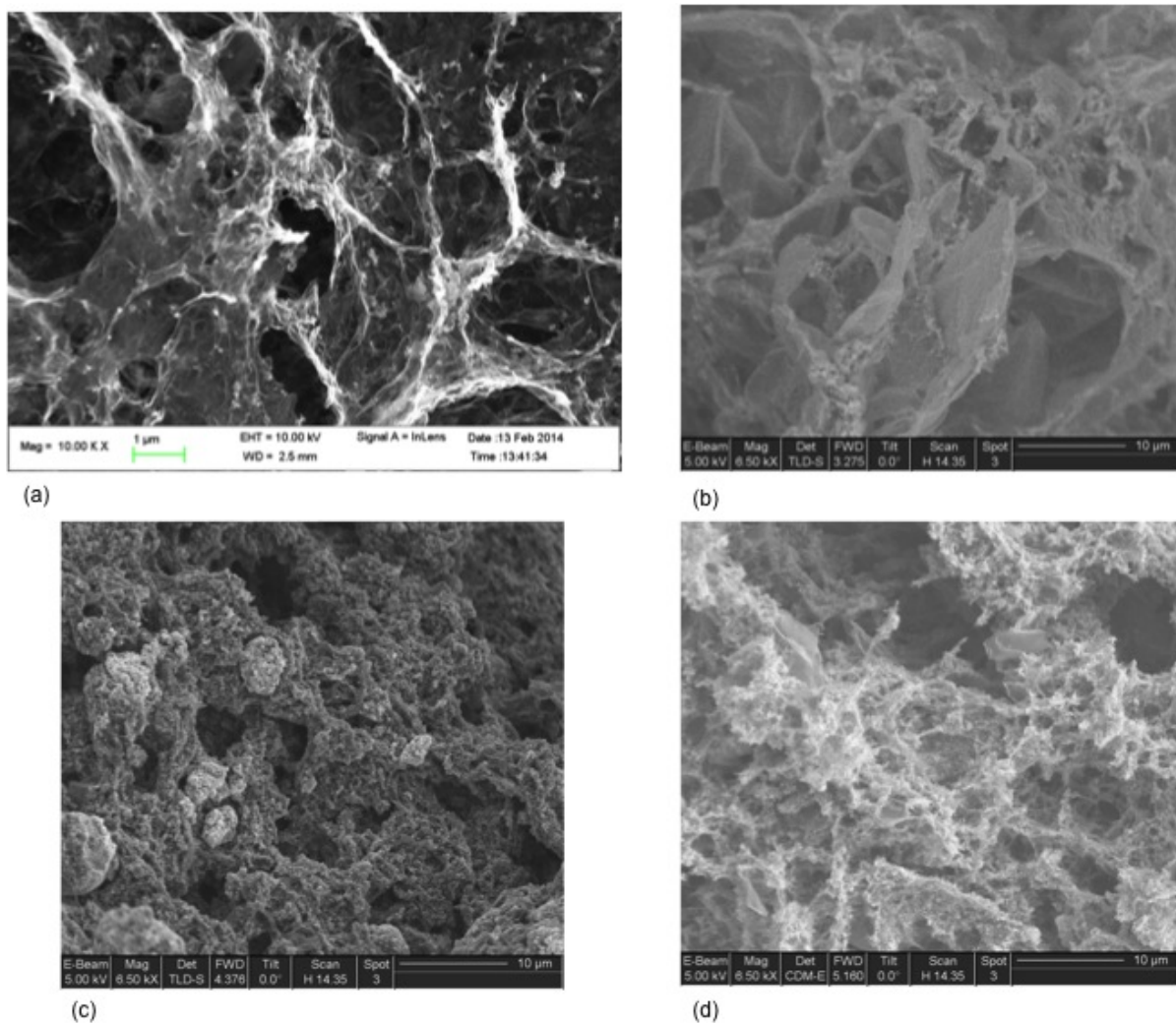


Figure 5.23 SEM picture at 6.5 kV of rGO/TiO<sub>2</sub> composites with different ration of graphene to TiO<sub>2</sub> (a) 5:1 (b) 1:1 (c) 1:3 and (d) 1:4.